

A comparison methodology for measured and predicted displacement fields in modal analysis

C.M. Sebastian^a, E. Lopez-Alba^b, E.A. Patterson^a

^a*School of Engineering, University of Liverpool, Liverpool, UK*

^b*Department of Mechanical Engineering and Mining, Campus las Lagunillas, University of Jaén, Spain*

Abstract

Recent advances in experimental mechanics have enabled full-field measurements of deformation fields and - particularly in the field of solid mechanics - methodologies have been proposed for utilizing these fields in the validation of computational models. However, the comparison of modal shapes and the path from the undeformed shape to the deformed shape at the extreme of a vibration cycle is not straightforward. Therefore a new method to compare vibration data from experiment to simulations is presented which uses full-field experimental data from the entire cycle of vibration. Here, the first three modes of vibration of an aerospace panel were compared, covering a frequency range of 14-59 Hz and maximum out-of-plane displacements of 2 mm. Two different comparison methodologies are considered; the first is the use of confidence bands, previously explored for quasi-static loading, the second is the use of a concordance correlation coefficient, which provides quantifiable information about the validity of the simulation. In addition, three different simulation conditions were considered, representing a systematic refinement of the model. It was found that meaningful conclusions can be drawn about the simulation by comparing individual components of deformation from the image decomposition process, such as the relative phase and magnitude. It was ultimately found that the best performing model did not entirely fall within the confidence bounds for all conditions, but returned a concordance correlation coefficient of nearly 70% for all three modes.

Keywords: validation, modal analysis, digital image correlation, Tchebichef, shape descriptor

1. Introduction

Modal analysis involves establishing the fundamental frequencies and the corresponding deformation shapes of structures during excitation. The

Email address: c.sebastian@liv.ac.uk (C.M. Sebastian)

analysis can be performed by modeling and/or experiment; and it is good practice to validate the predictions from a model using the measurements from experiments. Validation has been formally defined, by a number of guides [1, 2, 3], as establishing the extent to which a model is a reliable representation of the real world. In modal analysis, it is straightforward to compare the resonant frequencies predicted by a model to those measured in experiments. However, the comparison of modal shapes and the path from the undeformed shape to the deformed shape at the extreme of a vibration cycle is less straightforward and becomes more challenging when more complex excitation is present, such as acoustic loading. Recent advances in experimental mechanics have enabled measurements of deformation fields and, in the field of solid mechanics, methodologies have been proposed for utilizing these fields in the validation of computational models [4, 5]. However, the extension of these methods to include the temporal as well as the spatial domain during cyclic or vibration loading has not been explored and forms the focus of this study.

While the use of full-field methods of experimental strain analysis is gaining momentum in vibration analysis, there remain issues associated with the capture of data during fast events which require the use of stroboscopic illumination or expensive high-speed cameras. In addition, it presents new challenges in performing a meaningful comparison with predictions from a simulation due to the large quantity of data and issues with alignment of the coordinate systems, scaling, and interpolation. Therefore, the quantitative comparison of measured and predicted deformation fields for a vibrating component is especially challenging, as it encompasses all of these issues. Hence, the objective of this study was to integrate an elegant technique for data acquisition with an efficient and comprehensive validation methodology to provide an innovative approach to establishing the degree to which the predicted results were a reliable representation of the measured results from an experiment.

Over the past 15 years, a number of publications have addressed the need for verification¹ and validation² of computational models. In 1998, the American Institute for Aeronautics and Astronautics (AIAA) published a guide for the computational fluid dynamics community [1]. The Department of Defense has published several iterations of instructions regarding Modeling and Simulation, Verification, Validation, and Accreditation activities, the latest of which was issued in 2009 [2]. In 2005, the Clinical Biomechanics journal issued an editorial statement which defined minimal requirements for


¹verification is defined as “the process of determining that a computational model accurately represents the underlying mathematical model and its solution” [6].

²validation is defined as “the process of determining the degree to which a model is an accurate representation of the real world from the perspective of the intended uses of the model” [6].

a numerical study to be considered for publication [3] and at about the same time the solid mechanics community developed the Guide for Verification and Validation in Computational Solid Mechanics (ASME V&V) [6], which incorporates material published by Oberkampf and his co-workers [7] and provides a framework as well as defining terminology to create a standardized language [8]. Very recently in Europe, a CEN Workshop Agreement has been developed, which provides a protocol for performing a validation process for a computational solid mechanics model [5]; however, the protocol does not address validation of time-varying deformation fields.

Quantitative comparisons between the outcomes from a simulation and experiment should involve a metric that provides an indication of the level of confidence associated with the agreement between the outcomes, taking into account the error and respective uncertainties. An examination of the literature published in the last ten years reveals that a common approach to comparing measured and predicted data is to plot them together on the same graph for a section through the component [9, 10]. Typically, a metric is not used when performing this type of comparison and instead, the extent of the agreement is judged qualitatively by how well the two plots match one another. However, to perform a simple quantitative assessment, the relative error between the two sets of data can be calculated by normalizing the difference between the datasets using the measured value [11]. The relative error metric can be effectively applied to point-by-point comparisons and an algebraic sum or mean relative error used for a simple series of data points, but is not very effective or efficient for more complex comparisons. For example, it is not a good choice to compare tensors, or data with time or spatial components; and, the relative error becomes undefined as the measured value approaches zero. Information-rich data fields present similar challenges, and so the comparison is still often reduced to checking a few points rather than using the full data field, e.g. [12]. Recently, the authors proposed a quantitative procedure for comparing fields of deformation, strain or stress data using feature vectors composed of shape descriptors to describe measured and predicted fields [4]. A number of shape descriptors are available including an orthogonal descriptor based on the Zernike polynomials, which was described by Teague [13]. The Zernike descriptor is continuous and valid over a circular domain. An alternative discrete, orthogonal descriptor based on the Tchebichef polynomials was described by Mukundan *et al.* [14], which unlike the Zernike descriptor, is not invariant to rotation; however, the fact that it is discrete and valid over a rectangular domain makes it well-suited to measured and predicted data fields of strain and displacement. Wang and Mottershead have provided an overview of the different shape descriptors as well as some other methods of image decomposition along with their respective advantages and disadvantages [15]. They noted that the Tchebichef moments are better suited to detecting global features, while Krawtchouk moments are suited to detecting local features

[16]. Wang and his colleagues have used a variety of shape descriptors to tackle full-field data from various engineering problems. They used a modified Zernike descriptor to compare the measured strain field around a hole in a plate loaded in tension to the results from a computational model [17]. In addition, they applied the Tchebichef moments to represent mode shapes resulting from vibration measurements during finite element model updating [18], and an adaptive geometric moment descriptor for the vibration analysis of a car hood liner [19]. The adaptive geometric moment descriptor was also used to track the evolution of damage to the car hood liner subjected to an impact from a high-speed projectile [20]. An alternative approach to comparing data fields from modal analysis has been taken by Allemang et al. who used Principal Component Analysis (PCA) to compare two sets of experimental data from frequency testing of an automobile chassis [21].

In this study, the use of a generic decomposition process based on Tchebichef descriptors, which was used previously to compare strain fields in a composite panel subjective to static compressive loading [22], has been extended into the temporal or phase domain for use in the modal analysis of a prototype aircraft panel. In the experiments, pulsed-laser illumination has been used to address the challenge of capturing the changing deformation field of the panel resulting from the vibration excitation. The out-of-plane (z-direction) displacement field was measured using pulsed laser digital image correlation (PL-DIC) while exciting the panel at its first three resonances. The measured displacement fields were compared to those predicted by a modal frequency response simulation using a Finite Element (FE) analysis . The model was progressively refined to allow the impact of changes in the modeling conditions to be seen in the comparison metrics. Our intention is to illustrate the efficacy of the proposed methodology for comparing predicted and measured datasets and its usefulness as a diagnostic tool; hence we intentionally present predictions from less-than-perfect models. Data fields were captured in $\pi/10$ (18°) phase increments over the entire 2π cycle of vibration for both the simulation and the experiment. The measured and predicted displacement fields at each phase step were compared using image decomposition with the Tchebichef descriptor and the minimum measurement uncertainty in the measured data was used to aid an evaluation of the validity of the model.

2. Experimental Procedure

2.1. Apparatus

The panel used in these experiments was an 800 mm by 400 mm prototype aerospace component that had been milled from a single block of 7075 aluminum. The panel was suspended by string from a portal frame mounted on an optical table. A speckle pattern was applied with paint: first with a base layer of white and then the speckle provided using a sponge

to dab on the black paint. Instead of the hand-painted sponge pattern, a computer-generated printed pattern could have been bonded to the panel but there were concerns about disbonding during the excitation. The use of spray-painted pattern was not viable because of the relatively large speckle required, based on the guidance provided by Sutton [23]. Pictures of the panel in the experimental setup are shown in figure 1.

The design of the setup, including the excitation location and frequencies, was based in part on the results obtained from the modal analysis described in the next section. The experimental data was acquired at the first three natural frequencies, which were the first torsion mode (14 Hz), first bending mode (44 Hz), and a combined mode (59 Hz). The excitation was provided by an electrodynamic shaker (V100, DataPhysics, San Jose, CA) which was attached to the panel with a stinger (M4 300mm stainless steel rod) through a bolted connection.

A function generator was used to control the excitation at the required frequency and was connected to the shaker via an amplifier. The amplitude of the vibration was measured using a laser vibrometer (OFV-503 and OFV-2500, Polytec GmbH, Waldbronn, Germany) aimed at the attachment point of the stinger as shown in figure 2. **The laser vibrometer was used to measure the amplitude of the vibration as it has a calibration certificate, which provides traceability in its measurements back to a national standard.**

Images of the vibrating panel were captured using a Pulsed-Laser Digital Image Correlation (PL-DIC) system based on a pair of Firewire cameras with 1624x1234 pixels (Stingray F-201B, AVT GmbH, Stradtrda, Germany). The cameras were fitted with a matched pair of 8mm lenses (Cinegon 1.4/8, Schneider) set to an f-stop of 5.6, which provided an image magnification of approximately 3.1 pixels/mm. **The PL-DIC system consisted of a laser (Nano L-200-10, Litron, Rugby, England) with a four nanosecond pulse duration and wavelength of 532 nm which was fitted with a lens to expand the beam to illuminate the entire panel. The pulsed laser was used in a stroboscopic fashion, triggered at the same time as the cameras to essentially “freeze” the motion of the panel.**

The PL-DIC system is able to capture the periodic motion of a vibrating component by phase shifting the image acquisition relative to the excitation. In order to do this the excitation signal from the function generator has to be routed to the timing box of the DIC system (Dantec Dynamics, Ulm, Germany), which produces the appropriate phase offset to trigger the cameras and the pulsed laser. Figure 3 shows how the image acquisition was shifted relative to the vibration signal. A total of 20 images were captured in this fashion at $\pi/10$ (18°) phase increments, covering a full 2π (360°) cycle.

The image correlation was performed using a subset or facet size of 25 pixels and an offset or overlap of 21 pixels. **In order to obtain an indication of the noise floor in the setup, a series of ten images were captured with the**

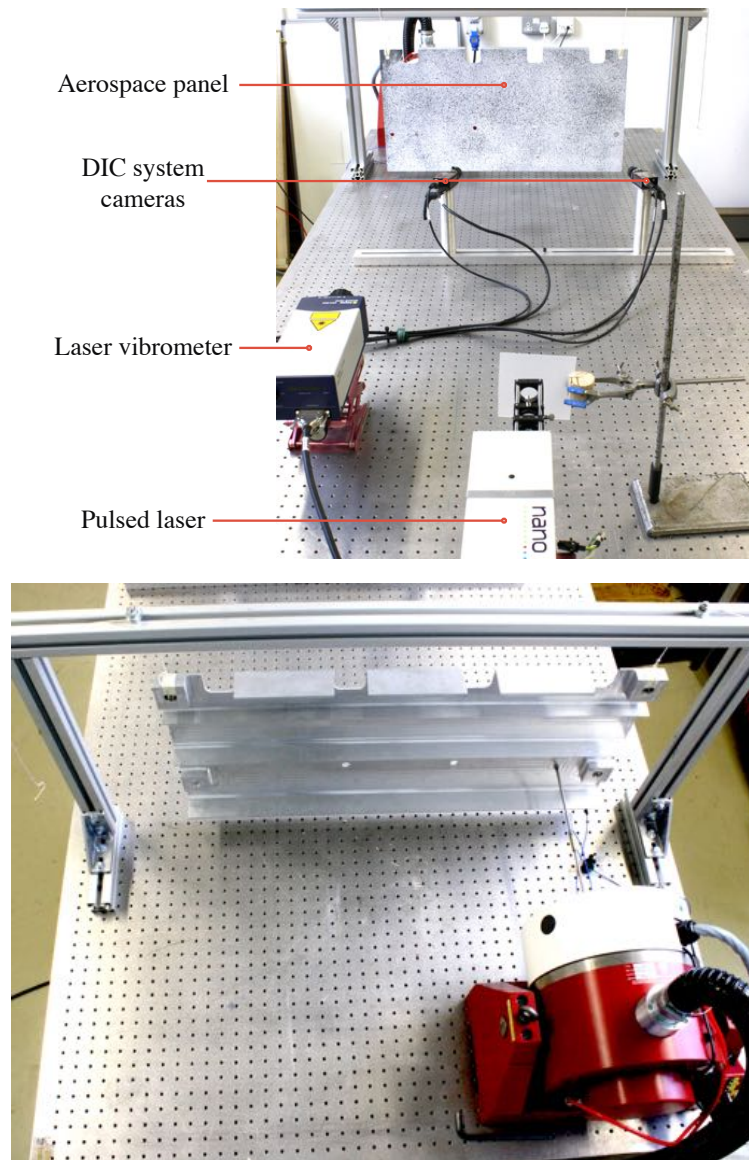


Figure 1: Picture of the front of the experimental setup showing the cameras, laser vibrometer, and pulsed laser (top) and the back side of the panel showing the attachment to the shaker (bottom).

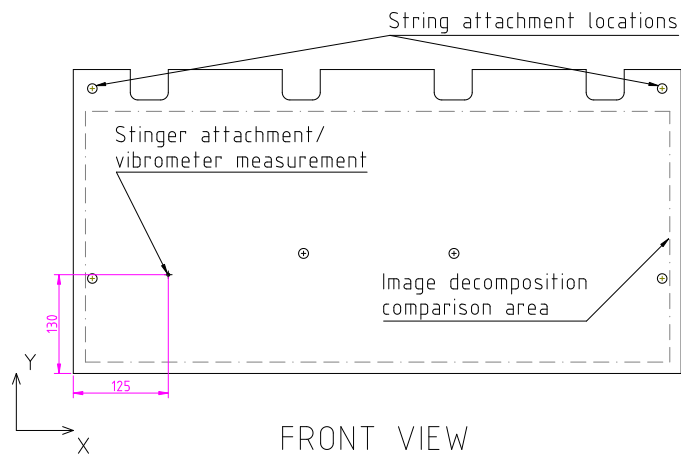


Figure 2: Front view of the panel showing the stinger attachment position and the comparison area for the image decomposition.

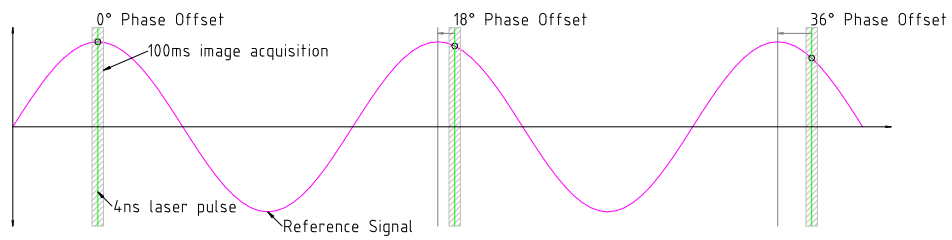


Figure 3: A graphical representation of the phase-stepping that the PL-DIC system performs to capture the motion of an object undergoing periodic vibration.

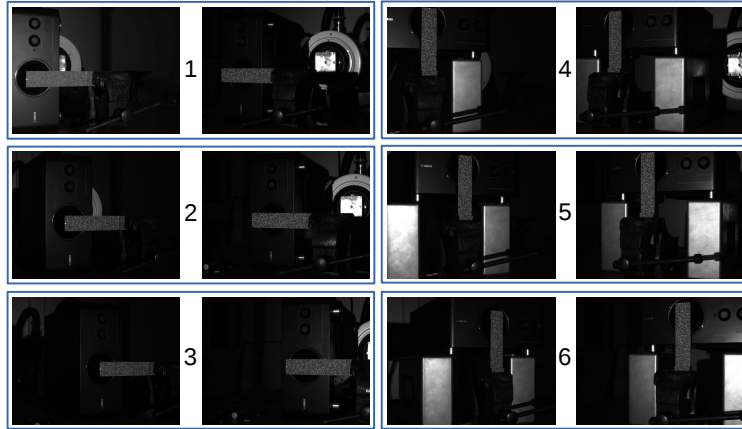


Figure 4: Images captured by the PL-DIC system of the calibration cantilever at six different positions in the field of view. The cantilever is shown horizontal in locations 1 to 3 and vertical in 4 to 6.

panel in a static configuration. The images were then processed using the DIC software to find the mean value of each of the displacement components. These were found to be approximately 2 microns in-plane, and 10 microns out-of-plane.

2.2. Dynamic calibration

A dynamic calibration was performed following the procedure described by Hack *et al.* [24] in order to establish the minimum measurement uncertainty. A 160 mm x 40 mm x 4 mm thick cantilever machined from a single aluminum block was excited acoustically and its out-of-plane displacement field was captured with the PL-DIC system. Acoustic excitation was used to avoid contact with the reference material causing a disturbance to its deformed state relative to the analytical solution. The reference value was obtained from a laser vibrometer calibrated against the national standard for length measurement.

During the procedure, the cameras were left in the exact same position as they were for the measurement of the aerospace panel. This was done to assess the particular setup, which included such things as the positions of the cameras as well as the setup the lenses and lighting. Consequently, the cantilever did not fill the field of view used for the experiments on the panel as it was only 160 mm long. Ideally, a larger cantilever would have been manufactured that had larger dimensions to fill the field of view. However, a practical approach was taken by using the standard cantilever and instead moving it around to six different locations in the field of view. Figure 4 shows the images from both cameras at each of the six calibration locations. Measurements were taken with the cantilever in both a horizontal

and vertical orientation at each location, to check that the uncertainty was the same in both directions. The results are summarized in table 1 and compared to those obtained previously with the high-speed DIC system [24]. It should be noted that the image magnification was slightly less than half that achieved with the high-speed system, as a result of increasing the field of view for the larger aerospace panel. The absolute uncertainty expressed in microns and the relative uncertainty in percent are also shown in table 1.

	Measured amplitude (μm)	$u_{cal}(w)$ (μm)	Relative uncertainty (%)
High-speed [24]	290	2.9	1.0
High-speed [24]	90	2.5	2.8
PL-DIC	250	4.0-4.7	1.6-1.9

Table 1: Comparison of the uncertainty from the high speed cameras (from Hack *et al.* [24]) and the PL-DIC, where $u_{cal}(w)$ is the uncertainty in the measurement. The last column gives the uncertainty expressed as a percentage of the measured amplitude of vibration from the calibration process.

3. Modeling details

3.1. Initial eigenvalue analysis

Initially to support the experiment design, an eigenvalue analysis was performed, using a commercial FE package (Altair Optistruct, MI USA), to identify the natural frequencies and corresponding mode shapes for the panel in the absence of any constraints or boundary conditions. The mesh, shown in figure 5, was created manually using 170,000 first order hex elements with 8 nodes per element. For the purposes of this study, it was not necessary to have a perfect model, as the emphasis is on the validation procedure and so no model refinement was performed. The modulus of the material was assumed to be 67 GPa with a Poisson’s ratio of 0.33, and density of 2850 kg/m^3 . The deformed out-of-plane shape of the first three eigenmodes from this analysis are shown in figure 5.

3.2. Modal response analysis

Subsequent to the eigenvalue analysis, a modal frequency response was performed to determine the full-field displacement of the panel subjected to the same loading as was measured during the experiment with the laser vibrometer. An enforced displacement constraint was applied to 12 nodes on the back of the panel at the location of the stinger from figure 2. These nodes were also constrained in the x- and y-directions, and rotation about the z-axis. The amplitude of the enforced displacement at each mode was measured by the laser vibrometer and is listed in table 2. At the first natural

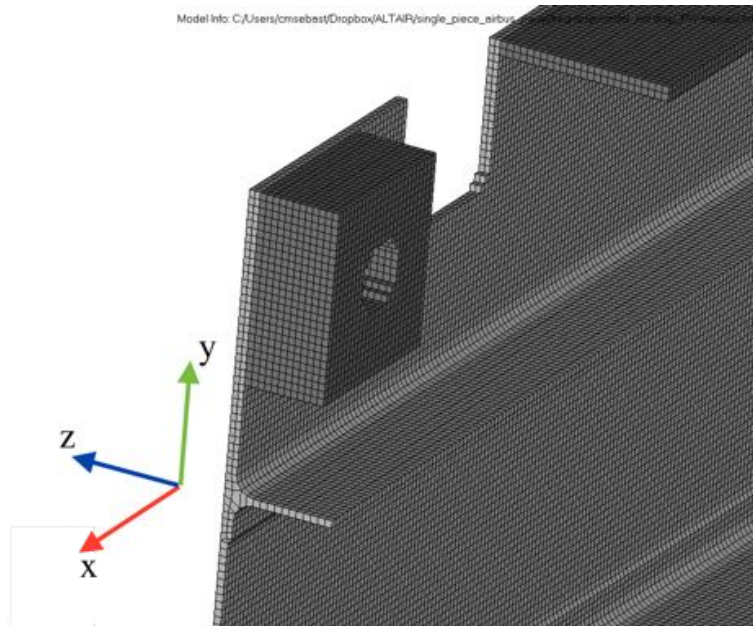


Figure 5: Close-up of the 3-D mesh used for the FE simulations.

	Stinger amplitude (mm)	Modal damping (%)
14 Hz (mode 1)	0.18	10
44 Hz (mode 2)	0.34	3
59 Hz (mode 3)	0.10	2

Table 2: Measured displacements at the attachment point of the stinger and the calculated damping coefficients.

frequency, a displacement of 0.18mm was applied, 0.34mm at the second, and 0.1mm at the third.

The model was subsequently ‘improved’ in two steps in order to examine the sensitivity of the validation process to changes in the model. The baseline model was as described above and had a constant damping coefficient of 0.01 for all modes. This model was refined by introducing modal damping, meaning that a different value of the damping coefficient was applied for each mode. The values were found experimentally by using the half power method from the frequency response function. The half-power method has been used in a number of recent studies to estimate coefficients for lightly damped systems, for instance Trebuna and Hagara [25] and Ha *et al.* [26]. Using this method, the resulting damping coefficients were found to be 0.10 for the first mode, 0.03 for the second, and 0.02 for the third. Finally, an extra constraint was applied to simulate the panel hanging from the strings

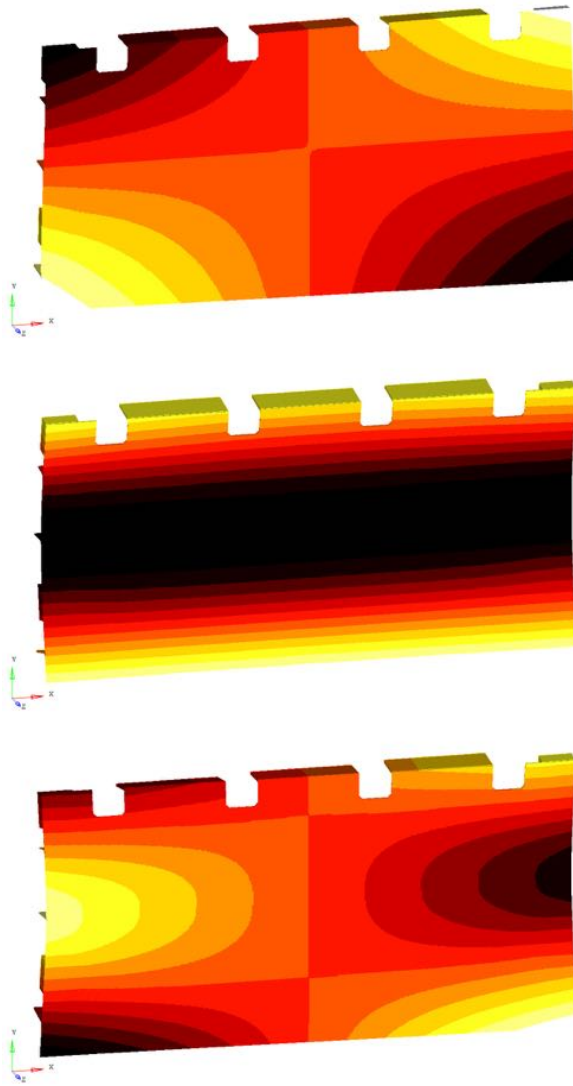


Figure 6: The deformed shape from the initial eigenvalue analysis for the first three modes of vibration.

and the four nodes in each of the upper corners of the panel were constrained from translating in the y-direction.

4. Results

4.1. Tchebichef decomposition

The out-of-plane displacement results obtained from the PL-DIC were compared to the simulation results using image decomposition. The data sets were rectangular and discrete so the Tchebichef descriptor (based on the Tchebichef polynomial) was used in the comparison. The Tchebichef moments, or shape descriptors of an MxN discrete image are given by [14],

$$T_{p,q} = \sum_{x=0}^{M-1} \sum_{y=0}^{N-1} \tilde{t}_p(x) \tilde{t}_q(y) f(x, y) \quad (1)$$

where $\tilde{t}_p(x)$ and $\tilde{t}_q(y)$ are the normalized Tchebichef polynomials

$$\tilde{t}_p(x) = \frac{\tilde{t}_p(x)}{\sqrt{\tilde{\rho}(p, M)}}, \quad \tilde{t}_q(y) = \frac{\tilde{t}_q(y)}{\sqrt{\tilde{\rho}(q, N)}} \quad (2)$$

and,

$$\tilde{\rho}(p, M) = \frac{M \left(1 - \frac{1}{M^2}\right) \left(1 - \frac{2^2}{M^2}\right) \dots \left(1 - \frac{p^2}{M^2}\right)}{2p + 1} \quad (3)$$

The discrete Tchebichef polynomials are given by,

$$t_n(x) = n! \sum_{k=0}^n (-1)^{n-k} \binom{N-1-k}{n-k} \binom{n+k}{n} \binom{n}{k} \quad (4)$$

A graphical representation of the first ten surfaces generated from the polynomial are shown in figure 7. The measured and predicted displacements fields were treated as images and decomposed using discrete Tchebichef polynomials to produce a feature vector representing the data from the experiment, S_E , and a feature vector representing the data from the simulation, S_M . Each of these vectors contained 50 elements, which are the moments or shape descriptors from the decomposition process. It is typically not necessary to use all of the moments generated in a decomposition process to accurately describe an image and in this study only the most significant moments were retained in the feature vector following the approach applied by Wang *et al.* [15]. The elements of the feature vector representing the data from the experiment, S_E , were sorted in descending order of magnitude, and the five largest retained. The vector was normalized by dividing each of the elements by the absolute value of the magnitude of the vector, as shown in equation 5.

$$\text{vector magnitudes} = \frac{S_{Ek}}{\sum |S_E|} \quad (5)$$

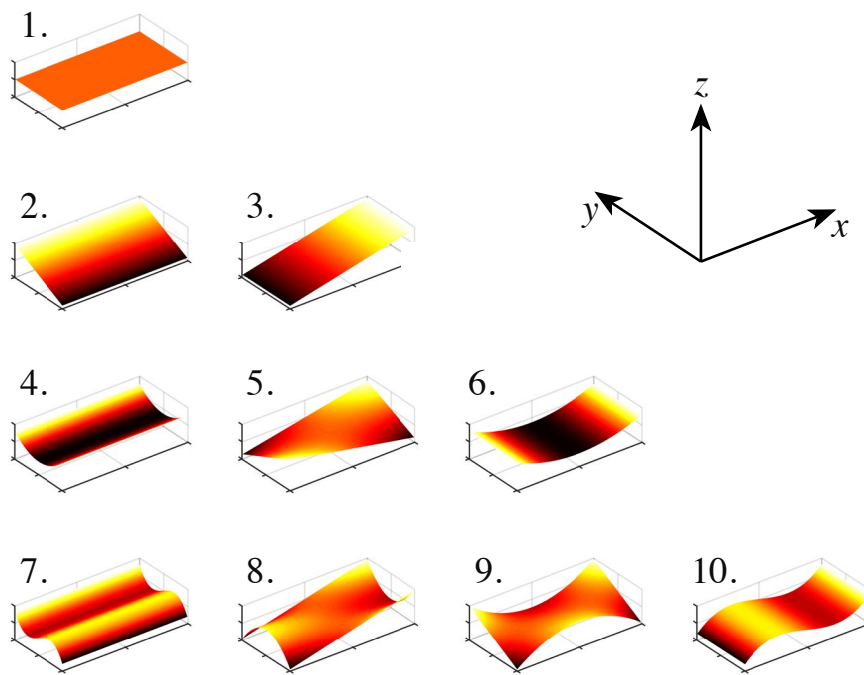


Figure 7: Graphical representation of the kernels of the first ten Tchebichef shape descriptors.

Finally, the quality of the representation of the original data field by the feature vector was checked by reconstructing the data field and assessing the difference between the original and reconstructed data fields using the squared residual,

$$u^2 = \frac{1}{n} \sum_{i,j}^n (\hat{I}(i, j) - I(i, j))^2 \quad (6)$$

where $\hat{I}(i, j)$ is the reconstructed matrix from the original data, $I(i, j)$. The approach recommended in CEN CWA 16799:2014 [5] was adopted so that the residual, u must not be greater than the minimum measurement uncertainty and that there should not be any clusters of pixels with residuals greater than $3u$, where a cluster is defined as a group of adjacent pixels comprising 0.3% or more of the total of number of pixels in the data field. The total uncertainty of the feature vector representing the experimental data field, $u(S_E)$, is given by a combination of the uncertainty from the reconstruction, u and the minimum measurement uncertainty from the calibration, u_{cal} :

$$u(S_E) = \sqrt{u_{cal}^2 + u^2} \quad (7)$$

where u_{cal} was found from the calibration procedure described in section 2.2.

5. Data comparison

The data fields measured with the DIC are shown in figure 8 and comprise the majority of the surface of the panel, excluding the discontinuities along the top edge. While it is possible to decompose data fields containing discontinuities, it requires customization of the shape descriptors [17] which introduces additional uncertainties and renders the process specific rather than generic. Hence, it was decided to extract a representative region of data from each data field using the rectangle defined in figure 2. The comparison process used in the validation described here could be extended by tiling the surface of the panel using similar rectangles following the procedure used by Lampeas *et al.* [27] for an I-beam subject to a static load. A total of 20 sets of data were compared for each of the three modes, covering a phase range of zero to 2π in $\pi/10$ increments. For each of the first three natural frequencies, the elements of the feature vectors representing the measured and predicted data fields have been plotted against each other during a vibration cycle in figures 8-10 for the baseline, modal damping and string constrained models respectively. **Each moment in the feature vector representing the measured data field has been plotted against its corresponding value in the feature vector representing the predicted data field. This has been performed for the 20 data sets acquired during an excitation cycle and the locus of points for each moment forms a loop on the graph with the measurement result**

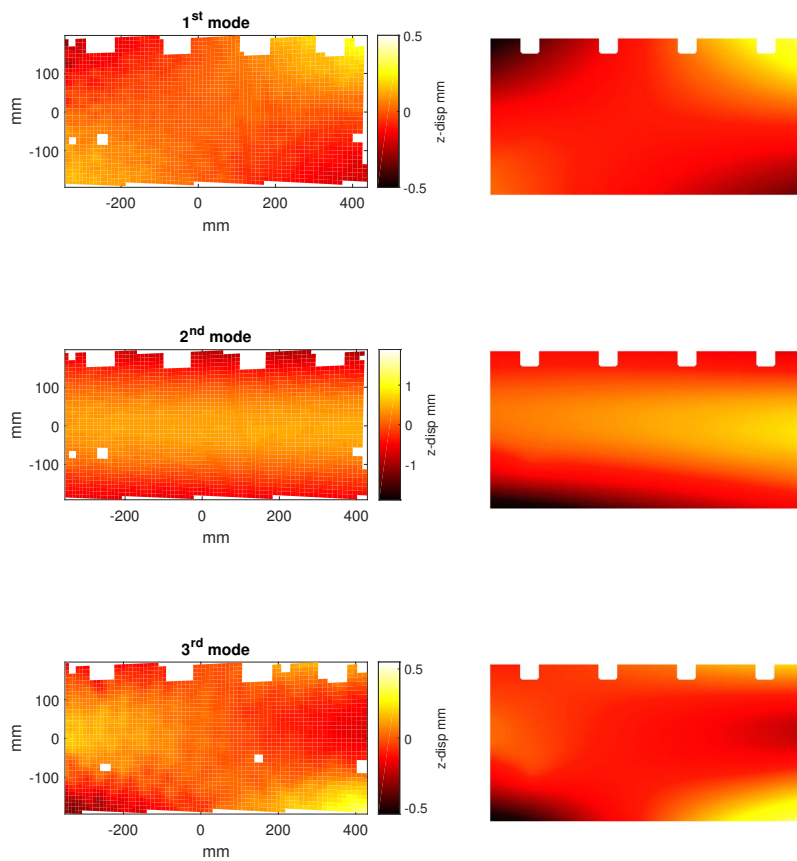


Figure 8: The measured (left) and predicted (right) out-of-plane displacement fields. The predictions shown in this figure were made using the model with modal damping but without string constraints.

acquired at zero phase shown by an open circle symbol. Perfect agreement between the experiment and model would result in all of the points lying along a straight line of gradient of unity. However, there will always be uncertainty in the data which will result in deviations from perfection and CEN CWA 16799:2014 [5] suggests that the model can be considered an acceptable representation of the experiment if all of the data on the plots in figure 9 fall within a zone either side of the straight line of gradient unity indicated by the dashed lines and defined by

$$S_M = S_E \pm 2u(S_E) \quad (8)$$

Hence, from the data in figures 9-11, it could be concluded that the most sophisticated model with modal damping and the string constraints is valid but only for the third mode of vibration.

6. Concordance

CEN CWA 16799:2014 [5] recommends the use of the concordance correlation coefficient as a measure or metric for the quality of representation of the experiment by the simulation data. Lin [28] proposed the concordance correlation coefficient, C_C , which has a measure of scatter, scale shift and location shift when comparing two data sets. It is the product of Pearson's correlation coefficient, r and a bias correction factor, C_B , i.e.

$$C_C = rC_B \quad (9)$$

Pearson's correlation coefficient can be considered to be a measure of the precision of the data and is given by

$$r = \frac{\sigma_{ab}}{\sigma_a \sigma_b} \quad (10)$$

where σ_a and σ_b are the standard deviations of the two data sets a and b , and σ_{ab} is their covariance. The bias correction factor can be considered a measure of accuracy and is combination of a scale shift, ν and location shift τ , such that

$$C_B = \frac{2}{\nu + \frac{1}{\nu} + \tau^2} \quad (11)$$

given, the scale shift is

$$\nu = \frac{\sigma_a}{\sigma_b} \quad (12)$$

and the location shift is

$$\tau = \frac{\mu_a - \mu_b}{\sqrt{\sigma_a \sigma_b}} \quad (13)$$

where μ_a and μ_b are the means of the two data sets. The concordance correlation coefficient was used to compare the individual elements of the feature

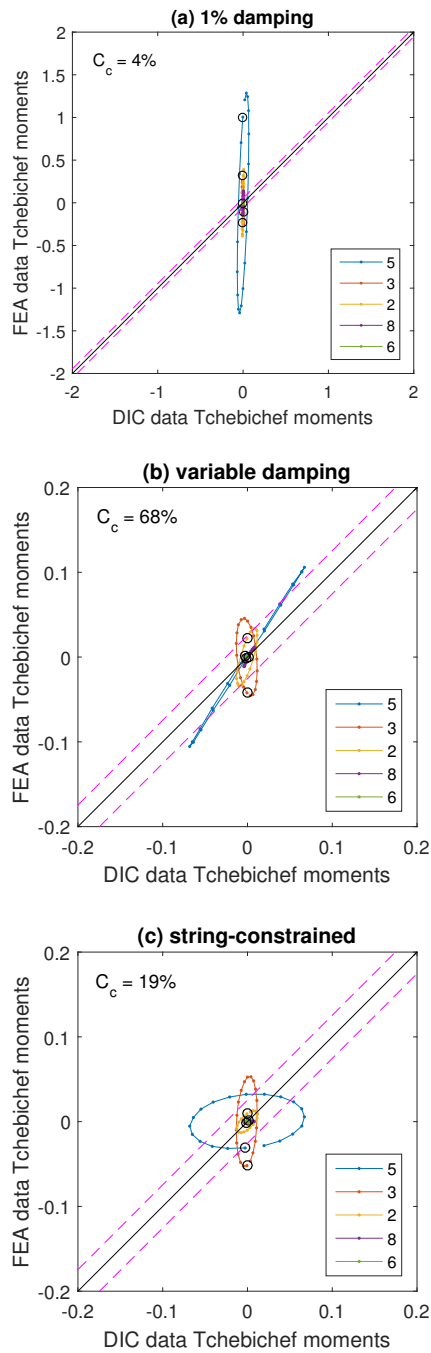


Figure 9: Time-varying comparison of the five largest Tchebichef moments (listed in rank order in the key) representing the measured (x-axis) and predicted (y-axis) displacement fields during a single cycle of vibration at the first natural frequency with zero phase data shown by an open circle symbol. The predictions were based on (a) the baseline model with constant damping, and the ‘improved’ models with (b) variable damping and (c) string constraint. The straight lines are defined by equation 8.

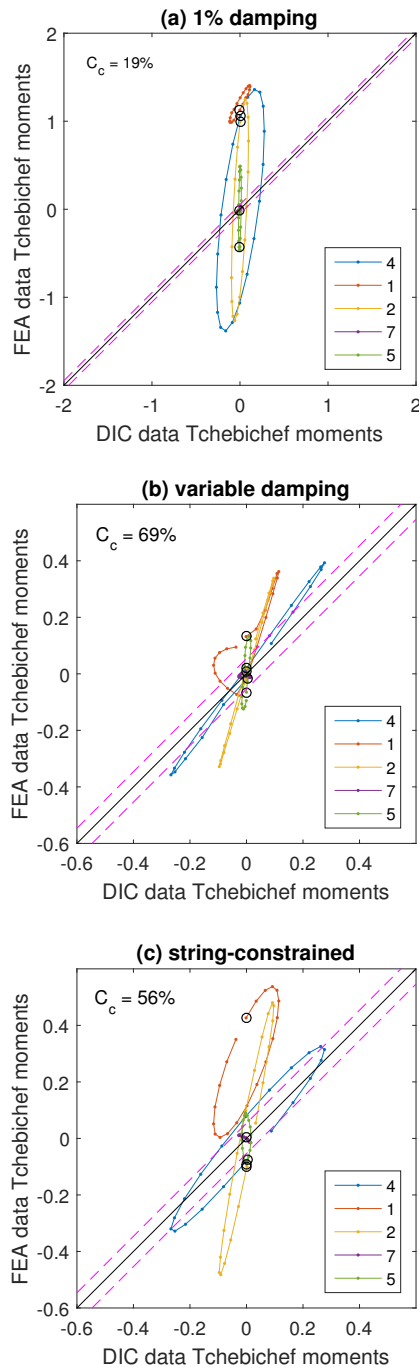


Figure 10: Time-varying comparison of the five largest Tchebichef moments (listed in rank order in the key) representing the measured (x-axis) and predicted (y-axis) displacement fields during a single cycle of vibration at the second natural frequency with zero phase data shown by an open circle symbol. The predictions were based on (a) the baseline model with constant damping, and the 'improved' models with (b) variable damping and (c) string constraint. The straight lines are defined by equation 8.

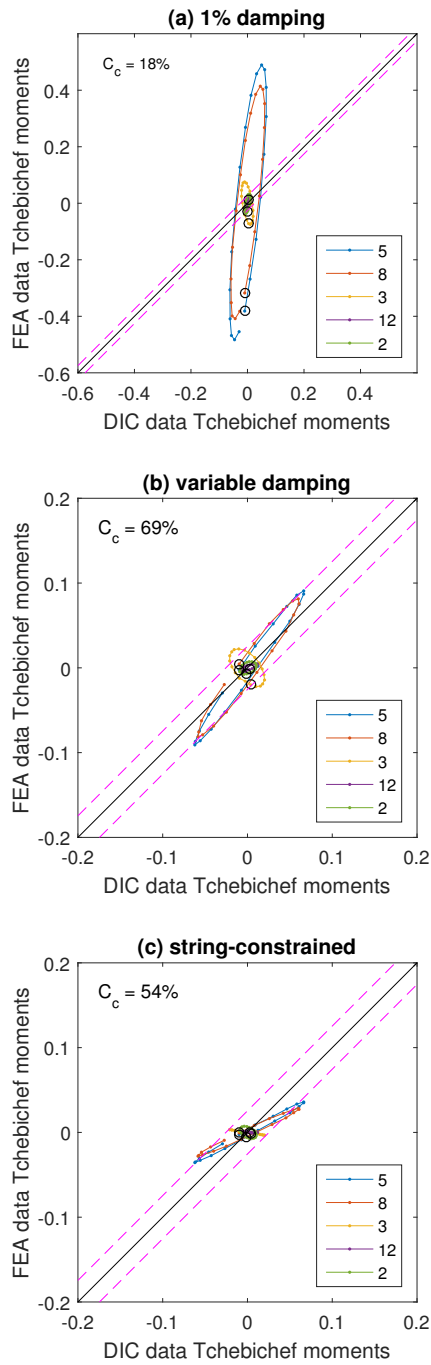


Figure 11: Time-varying comparison of the five largest Tchebichef moments (listed in rank order in the key) representing the measured (x-axis) and predicted (y-axis) displacement fields during a single cycle of vibration at the third natural frequency with zero phase data shown by an open circle symbol. The predictions were based on (a) the baseline model with constant damping, and the ‘improved’ models with (b) variable damping and (c) string constraint. The straight lines are defined by equation 8.

vectors over a vibration cycle at each resonant frequency. A weighted correlation coefficient was calculated by multiplying the individual correlation values by the magnitude of the feature vector value calculated using equation 5. The weighted values were then summed for the five moments used in the reconstruction, and then converted to a percentage of the maximum value possible if these five moments had a correlation coefficient value of 1. This percentage is reported in figures 9-11.

7. Discussion

The graphs in figures 9-11 follow the approach recommended by CEN CWA 16799:2014 [5] and permit a judgment to be made about the validity of the models. The approach employed here represents an advance on the earlier work incorporated into the CEN document because the comparison of the measured and predicted deformation fields is made over a period of time, i.e. the period of vibration. The loops formed by plotting the time-varying values of the individual Tchebichef moments provide additional information about the performance of the models relative to the experiment. At zero phase all of the moments would be expected to have a zero value because this corresponds to the undeformed state and would also be expected to return to this value at a phase value of 2π , i.e. the end of the cycle. However, the latter does not always occur, for instance for the second mode a number of moments develop a path that is an open ellipse that does not pass through the origin on the graph. It would be expected that the moments exhibit cyclic variations in their magnitude during the vibration cycle in order to describe the cyclic variation in the out-of-plane deformation. If the measured and predicted deformation fields were similar, then the phase path of the moments would follow the straight line of gradient unity; yet, if the simulation underestimates the magnitude of the deformation then phase path of the moments would tend towards to rotate clockwise about the origin and vice versa for an overestimate. When the comparison of the cyclic deformation is symmetric with respect to the extremes of the deformation then the phase path will follow the same straight line, i.e. ratio of the length of the minor to major axes of the phase path is close to zero. However, when the comparison is asymmetric about the extremes of the deformation then the phase paths will develop into an ellipse or even tend towards being circular. This asymmetric behavior can be observed to some extent in all three of the modes, but is particularly obvious in the string-constrained model at the first mode of vibration shown in figure 9(c). The difference is in moment #5, which represents a torsion of the panel. Compared to figure 9(b), which does not have the extra string constraint, the deformation predicted by the simulation is much less than that from the experiment, and lags behind. Hence, it is reasonable to suggest that the non-zero value of the ratio of the minor to major axes of these phase paths is indicative of these

components of the predicted deformation fields being out of phase with the experimental results. An exploration of the shape of these phase paths for the individual moments shown in figures 9-11 can be used as a diagnostic tool for improving the model.

It is difficult to identify an acceptable deviation from unity for the correlation coefficients but this is not important because they provide a comparative metric whereas the plots in figures 9-11 provide a means to decide on the acceptability or otherwise of the predicted data. In these latter plots the expanded uncertainty in the feature vectors representing the measured data fields is used to define a zone within which the data must lie if the predicted data fields are to be considered valid. In this study, the uncertainty present in the feature vectors representing the measured deformation fields is quite small. The minimum measurement uncertainty obtained from the calibration procedure was only 1% of the out-of-plane displacement measurement (see table 1) and the measurement uncertainty was calculated as the product of this relative uncertainty and the maximum displacement range measured (see table 2). The uncertainty from the reconstruction process was of the order of 5 to 10 microns which, when combined with the measurement uncertainty using equation 7, gave an unexpanded uncertainty of 18 microns for the first mode, 38 microns for the second mode, and 35 microns for the third mode, compared to maximum z-displacement of 2, 0.4, and 1 mm respectively. The concordance correlation coefficient was introduced as an alternative way to assess the performance and validity of the model when a cycle is involved. The expanded uncertainty bands, defined by equation 8 from [5] give a quick indication and a go/no-go type of approach. However, in this example, where several different simulation conditions are considered, the approach does not provide any quantitative information regarding the quality of each simulation, and so it is difficult to compare the relative merits of each model.

One such example of this is shown in figure 11, in the comparison of the variable damping (b) and string constrained (c) models. Both of these examples nominally fall within the confidence bounds, indicating that either would be a suitable simulation. By using the concordance correlation coefficient, it is possible to determine some distinction between the models. In this case the variable damping model has a C_C of 69% compared to 54% for the string-constrained model. It could be argued that the half-power method is not ideal to obtain damping coefficients for a lightly-damped structure. However, these results suggest that it gives damping coefficients that lead to acceptable predictions.

In general, the baseline model with constant damping is a poor representation of the experiment. The loops are stretched along the FE-scale, indicating that the 1% damping coefficient used was too low, resulting in large predicted deformations from the simulation. None of the results fall within the confidence bands for any of the three modes, and the concordance

percentage varies from only 4% to at most 19%.

A refinement of the model by using variable damping is presented in the center panel of figures 9-11. For the first mode, the largest moment coefficient is #5, which corresponds to torsional deformation of the plate (see figure 7). This is well captured by the simulation, but falls slightly out of bounds at the extremes of vibration. In addition, one of the rigid body components (#3) falls outside the bounds. Similarly, for the second mode, the largest moment coefficient is this time #4, and also falls out-of-bounds at the extremes. The other moments are not as well represented by the simulation, as they are larger along the FE-axis direction of the plot. The results for the third mode fall within the confidence bounds with the exception of moment #3, which represents a tilt of the panel. The loop for this moment is perpendicular to the unity line, indicating that this component is 180 degrees out-of-phase with the experiment. The concordance correlation percentages are high for this simulation condition, at 68% for the first mode and 69% for the second and third modes.

The further refinement to the model was the addition of an extra constraint at the top of the panel to simulate the potential boundary condition imposed by the strings attaching the panel to the frame, and the results are shown in the bottom panel for each mode in figures 9-11 respectively. For the first mode of vibration, this had the greatest effect on moment #5, which was greatly reduced in magnitude and its loop squished into an oblong ellipse, causing the majority of it to fall outside the confidence bounds. The concordance percentage was also greatly reduced as a consequence of this change, going from 68% to 19%. The impact on the second mode was slightly more complicated. The largest moment coefficient, #4, was not affected much, but there was a shift in the overall magnitude (#1), which stays completely positive for the simulation during the cycle. The tilting component in the simulation (#2) has also increased, which is not surprising considering that the constraint was only imposed on the top edge of the panel. Overall the change had the effect of reducing the concordance correlation percentage to 56% from 69%. Finally, the results for the third mode nominally fall within the bands for both this condition and the variable damping condition. However, as was previously noted, the correlation coefficient is better for the variable damping model compared to the string constraint (69% vs. 54%).

8. Conclusions

A new approach to representing time- or phase-varying spatial fields of displacements during a vibration cycle has been developed and used for comparison of measured and predicted data. The inclusion of information about uncertainty in the measured data on the plots allows decisions about the acceptability of the predictions to be made. The use of the concordance

correlation coefficient allows the quality of the comparison to be quantified so that a conclusion about the validity of the predictions can be made. The process is enabled by treating the displacement fields as images that can be decomposed to feature vectors for which, in this study, the well-established Tchebichef polynomials have been used. It has been shown that by plotting the phase-variation of the measured and predicted elements of the feature vectors, that is the coefficients or moments of the polynomial, a series of phase paths are formed and their shape can be used as a diagnostic tool to refine the simulation. These processes have been demonstrated using a prototype aerospace panel excited at its first three modes.

Acknowledgements

Effort sponsored by the Air Force Office of Scientific Research, Air Force Material Command, USAF, under grant number FA8655-11-1-3083. The U.S. Government is authorized to reproduce and distribute reprints for Governmental purpose notwithstanding any copyright notation thereon. EAP is the recipient of a Royal Society Wolfson Research Merit Award.

References

- [1] AIAA, Guide for the verification and validation of computational fluid dynamics and simulations, Tech. Rep. G-077-1998, American Institute of Aeronautics and Astronautics, Reston, VA (1998).
- [2] DoD, Modeling and simulation verification, validation, and accreditation, Tech. Rep. DODI 5000.61, Department of Defense (2009).
- [3] M. Viceconti, S. Olsen, L.-P. Nolte, K. Burton, Extracting clinically relevant data from finite element simulations, *Clinical Biomechanics* 20 (5) (2005) 451 – 454. doi:DOI: 10.1016/j.clinbiomech.2005.01.010.
- [4] C. Sebastian, E. Hack, E. Patterson, An approach to the validation of computational solid mechanics models for strain analysis, *The Journal of Strain Analysis for Engineering Design* 48 (1) (2013) 36–47.
- [5] Comite Europeen de Normilisation (CEN), CWA 16799:2014 Validation of computational solid mechanics models, Tech. rep. (2014).
- [6] L. Schwer, H. Mair, R. Crane, Guide for verification and validation in computational solid mechanics, American Society of Mechanical Engineers, ASME V&V 10.
- [7] W. L. Oberkampf, T. G. Trucano, C. Hirsch, Verification, validation, and predictive capability in computational engineering and physics, *Applied Mechanics Reviews* 57 (5) (2004) 345–384. doi:10.1115/1.1767847.

- [8] L. Schwer, An overview of the PTC 60/V&V 10: Guide for verification and validation in computational solid mechanics, *Engineering with Computers* 23 (4) (2007) 245–252.
- [9] M. Greenwald, Verification and validation for magnetic fusion, *Physics of Plasmas* 17 (2010) 058101.
- [10] K. Solanki, M. Horstemeyer, W. Steele, Y. Hammi, J. Jordon, Calibration, validation, and verification including uncertainty of a physically motivated internal state variable plasticity and damage model, *International Journal of Solids and Structures* 47 (2) (2010) 186–203.
- [11] L. Schwer, Validation metrics for response histories: Perspectives and case studies, *Engineering with Computers* 23 (4) (2007) 295–309.
- [12] E. A. Patterson, P. Brailly, M. Taroni, High frequency quantitative photoelasticity applied to jet engine components, *Experimental Mechanics* 46 (2006) 661–668.
- [13] M. Teague, Image analysis via the general theory of moments, *JOSA* 70 (8) (1980) 920–930.
- [14] R. Mukundan, S. Ong, P. Lee, Image analysis by Tchebichef moments, *IEEE Transactions on Image Processing* 10 (9) (2002) 1357–1364.
- [15] W. Wang, J. E. Mottershead, Adaptive moment descriptors for full-field strain and displacement measurements, *The Journal of Strain Analysis for Engineering Design* 48 (1) (2013) 16–35.
- [16] P.-T. Yap, R. Paramesran, S.-H. Ong, Image analysis by Krawtchouk moments, *IEEE Transactions on Image Processing* 12 (11) (2003) 1367–1377.
- [17] W. Wang, J. E. Mottershead, C. M. Sebastian, E. A. Patterson, Shape features and finite element model updating from full-field strain data, *International Journal of Solids and Structures* 48 (11) (2011) 1644–1657.
- [18] W. Wang, J. E. Mottershead, A. Ihle, T. Siebert, H. Reinhard Schubach, Finite element model updating from full-field vibration measurement using digital image correlation, *Journal of Sound and Vibration* 330 (8) (2011) 1599–1620.
- [19] W. Wang, J. E. Mottershead, T. Siebert, A. Pipino, Frequency response functions of shape features from full-field vibration measurements using digital image correlation, *Mechanical Systems and Signal Processing* 28 (2012) 333–347.

- [20] R. L. Burguete, G. Lampeas, J. E. Mottershead, E. A. Patterson, A. Pipino, T. Siebert, W. Wang, Analysis of displacement fields from a high-speed impact using shape descriptors, *The Journal of Strain Analysis for Engineering Design*.
- [21] R. Allemang, M. Spottswood, T. Eason, A principal component analysis (PCA) decomposition based validation metric for use with full field measurement situations, in: *Model Validation and Uncertainty Quantification*, Vol. 3, Springer, 2014, pp. 249–263.
- [22] C. M. Sebastian, E. A. Patterson, D. Ostberg, Comparison of numerical and experimental strain measurements of a composite panel using image decomposition, *Applied Mechanics and Materials* 70 (2011) 63–68.
- [23] M. Sutton, J. Orteu, H. Schreier, *Image correlation for shape, motion and deformation measurements: Basic concepts, theory and applications*, Springer Verlag, 2009.
- [24] E. Hack, X. Lin, E. Patterson, C. Sebastian, A reference material for establishing uncertainties in full-field displacement measurements, *Measurement Science and Technology* 26 (7) (2015) 075004.
- [25] F. Trebuña, M. Hagara, Experimental modal analysis performed by high-speed digital image correlation system, *Measurement* 50 (2014) 78–85.
- [26] N. Ha, H. Vang, N. Goo, Modal analysis using digital image correlation technique: An application to artificial wing mimicking beetles hind wing, *Experimental Mechanics* 55 (5) (2015) 989–998.
- [27] G. Lampeas, V. Pasialis, X. Lin, E. Patterson, On the validation of solid mechanics models using optical measurements and data decomposition, *Simulation Modelling Practice and Theory* 52 (2015) 92–107.
- [28] L. I.-K. Lin, A concordance correlation coefficient to evaluate reproducibility, *Biometrics* (1989) 255–268.